Check for
updates

Properties of High-Frequency Type II Radio Bursts and Their Relation to the Associated Coronal Mass Ejections

A.C. Umuhire[1,2,3] · **N. Gopalswamy**[2] · **J. Uwamahoro**[4] ·
S. Akiyama[2,3] · **S. Yashiro**[2,3] · **P. Mäkelä**[2,3]

Abstract Solar radio bursts are often early indicators of space weather events such as coronal mass ejections (CMEs). In this study, we determined the properties of a sample of 40 high-starting-frequency (≥ 150 MHz) type II radio bursts and the characteristics of the associated CMEs such as width, location and speed during 2010–2016. The high starting frequency implies shock formation closer to the solar surface, which has important ramifications for the analysis of particle acceleration near the Sun. We found the CME heliocentric distances at the onset time of metric type II bursts range from 1.16 to 1.90 solar radii (Rs). The study was also extended to 128 metric type II bursts to include lower-starting-frequency events for further analysis. The projected CME heights range from 1.15 to 2.85 Rs. The lower starting frequency correspond to shocks forming at larger heights. A weak correlation was found between the type-II starting frequency and CME heights, which is consistent with the density decline in the inner corona. The analysis confirmed a good correlation between the drift rate and the starting frequency of type II bursts (correlation coefficient ~ 0.8). Taking into account the radial variation of CMEs speeds from the inner corona to the interplanetary medium, we observed the deviations from the universal drift-rate spectrum of type II bursts and confirmed the previous results relating type II bursts to CMEs.

Keywords Type II radio bursts · Coronal Mass Ejections · Shocks

1. Introduction

Type II radio bursts are slow-drifting and long-lasting radio emission produced by nonthermal electrons accelerated at shocks propagating through the solar corona and interplanetary medium (Nelson and Melrose, 1985; Mann, Classen, and Aurass, 1995; Zlotnik et al.,

✉ A.C. Umuhire
  angelaciany@gmail.com

1 College of Science and Technology, University of Rwanda, Kigali, Rwanda

2 NASA Goddard Space Flight Center, Greenbelt, MD 20771, USA

3 The Catholic University of America, Washington, DC 20064, USA

4 College of Education, University of Rwanda, Eastern Province, Rwanda

Springer

1998; Gopalswamy, 2000; Cliver et al., 2004; Schmidt, Cairns, and Lobzin, 2014). The accelerated electrons generate Langmuir waves, which get converted into electromagnetic radiation by the plasma emission mechanism first identified by Ginzburg and Zheleznyakov (1958). Currently, there is a common understanding that type II radio bursts are produced by shocks formed ahead of Coronal Mass Ejections (CMEs) moving with super-Alfvénic speeds (Gopalswamy et al., 2001a, 2009a). The CME height at the time of the type II burst onset indicates the height at which the CME becomes super-Alfvénic to drive a fast mode magneto-hydrodynamic (MHD) shock (Gopalswamy et al., 2013). More research studies on the comparison between type II bursts and CMEs became possible at the beginning of Solar Cycle 23, when CMEs could be observed using the Solar and Heliospheric Observatory (SOHO) mission.

Cliver et al. (2004) found that the leading edge of the 1997 November 6 CME was at 1.3 Rs at the time of the associated type II onset. Gopalswamy et al. (2009a) found an average CME height ∼ 1.5 Rs using Solar Terrestrial Relations Observatory (STEREO) CMEs and ∼ 2.2 Rs using SOHO CMEs at the onset of metric type II bursts. The projection effects were minimal as the type II burst originated from close to the limb. Gopalswamy et al. (2012, 2013) showed that the 2010 June 13 type II burst occurred precisely when the shock appeared in the Extreme Ultraviolet (EUV) images obtained by the Atmospheric Imaging Assembly (AIA, Lemen et al. (2012)) on board the Solar Dynamics Observatory (SDO). They found that the shock heights obtained were smaller than the ones obtained from Gopalswamy et al. (2009a) using Coronagraph 1 (COR1) data. Gopalswamy et al. (2013) analyzed 32 metric type II bursts in conjunction with the STEREO EUV and coronagraphic observations to minimize the projection effects and significant extrapolation. They found that the shock noses were located in the heliocentric distance range from 1.20 to 1.93 Rs.

The CME shock height at the type II onset can be measured in two different ways depending on the source location. The leading edge method can be used for limb events and the wave diameter method is applicable when the CME eruption occurs on the disk. More details on the measurement of CME shock heights can be found in Gopalswamy et al. (2013).

One of the important physical parameters of type II bursts is the drift rate, which is the rate at which the emission frequency changes with time. Previous studies established a universal relationship between the drift rate of type II bursts and the frequency of emission (Vršnak et al., 2001; Aguilar-Rodriguez et al., 2005; Gopalswamy, 2006a). They made a log-log scale scatter plot of the drift rate ($\frac{\Delta f}{\Delta t}$) and the emission frequency (f). The first set consisted of type II bursts observed by Radio and Plasma Wave experiment on board Wind spacecraft (WIND/WAVES, Bougeret et al., 1995) and International Sun-Earth Explorer-3 (ISEE-3) (Lengyel-Frey and Stone, 1989) in various spectral domains and the second data set of metric-to-kilometric (m-to-km) events from Gopalswamy et al. (2005). By combining the two data sets with metric type II data from Mann et al. (1996), they found that at higher frequencies the bursts have larger drift rates and the relation was applicable from m to km domains. Hence, they got a power-law relationship of the form $\frac{\Delta f}{\Delta t} \sim f^\epsilon$ where the power-law index $\epsilon \sim 2$. The analysis made by Aguilar-Rodriguez et al. (2005) shows that ϵ increases from m ($\epsilon \sim 1.4$) to km ($\epsilon \sim 2.3$) domains, respectively. One can infer that the variation is due to the changing shock speed. Close to the Sun (m domain) most CMEs are likely to be accelerating, while they are decelerating in the interplanetary (IP) medium. However, for purely km type IIs, the CMEs may be accelerating far into the IP medium (Gopalswamy et al., 2004). But generally, it is known that CMEs and shocks decrease in speed between the Sun and 1 AU (Gopalswamy, 2000) because of the drag force of the ambient medium acting on the CMEs (Gopalswamy et al., 2001b; Vršnak et al., 2001). The CME shock speed increases with increase of the drift rate ($\frac{\Delta f}{\Delta t}$) with the power law index

(ϵ). In contrast, it decreases with emission frequency due to local plasma density. From the CME shock speed relation derived in Gopalswamy et al. (2013), we see that the shock speed decreases with heliocentric distance.

In this study, 128 type II bursts are analyzed, with a special emphasis on the 40 high-frequency bursts to check the drift–frequency relationship. Previous studies considered events with lower starting frequencies (< 14 MHz), and upper starting frequency in metric domain ~ 140 MHz. Here we investigate type II bursts with starting frequency ≥ 150 MHz to check whether the universal drift rate–frequency relationship extends to high frequencies.

This paper is organized as follows: Section 2 describes the type II radio data and CME height–time measurements from the Large Angle and Spectrometric Coronagraphs (LASCO) and STEREO/COR1 and EUVI instruments. Several limb events in STEREO view were observed as disk events by SDO/AIA, which were used for confirmation of the STEREO measurements. The data processing methods are also discussed in this section. In Section 3, we present the drift–frequency characteristics of all analyzed type II bursts in comparison with those at high frequencies. This section also discusses CME evolution in space and time. For method verification, the analyzed data are compared with previously published data. Section 4 provides a summary and conclusions of the study.

2. Data and methods

The metric type II bursts considered in this study occurred during the period from 2010 to 2016, in the weakly active Solar Cycle 24. We checked the occurrence of type II burst as reported on the website of the Space Weather Prediction Center (ftp://ftp.ngdc.noaa.gov/STP/swpc_products/daily_reports/solar_event_reports/) and considered those which are having spectral data obtained by different ground-based radio spectrographs. We obtained the frequency range and their corresponding time directly using an online tool for measurement via https://cdaw.gsfc.nasa.gov/meetings/2017_mekelle/00_all_type2.html. For each type II burst, we identified the associated CME from STEREO and SOHO instruments that image in the corona in EUV and/or white light. By combining coronagraph and EUV images, we were able to track all CME sources to the solar surface. CME properties were obtained from the SOHO/LASCO CME catalog (Yashiro et al., 2004; Gopalswamy et al., 2009b) available online at: http://cdaw.gsfc.nasa.gov/. Figure 1 shows an example of a high-starting-frequency type II burst observed by the Green Bank Solar Radio Bursts (GBSRB) spectrometer and its associated CME observed by STEREO-B/EUVI instruments.

It is known that the drift rate of metric type II radio bursts is related to the speed of the underlying shocks and the density gradient in the solar corona (see, e.g., Gopalswamy, 2011). Therefore, the drift rate $\frac{\triangle f}{\triangle t} = \frac{f2-f1}{t2-t1}$ (where f2 is the type II starting frequency, f1 is the ending frequency. t2 and t1 are the corresponding times, respectively) at a given frequency is related to the velocity (V) of the source (Mann and Klassen, 2005; Aguilar-Rodriguez et al., 2005; Gopalswamy, 2006a) as follows:

$$V[\text{km/s}] = -\frac{2r}{\alpha} \frac{1}{f[\text{MHz}]} \frac{\triangle f[\text{MHz}]}{\triangle t[\text{s}]}.$$ (1)

Here r is the shock height expressed in solar radii, Rs $= 696\,000$ km and α is the exponent describing density (n) variation over the radial distance ($n \sim r^{-\alpha}$).

For the burst in Figure 1, the fundamental starting frequency of the type II burst in the dynamic spectrum was 420 MHz (f2) at 17:35:00 UT (t2). The ending frequency was
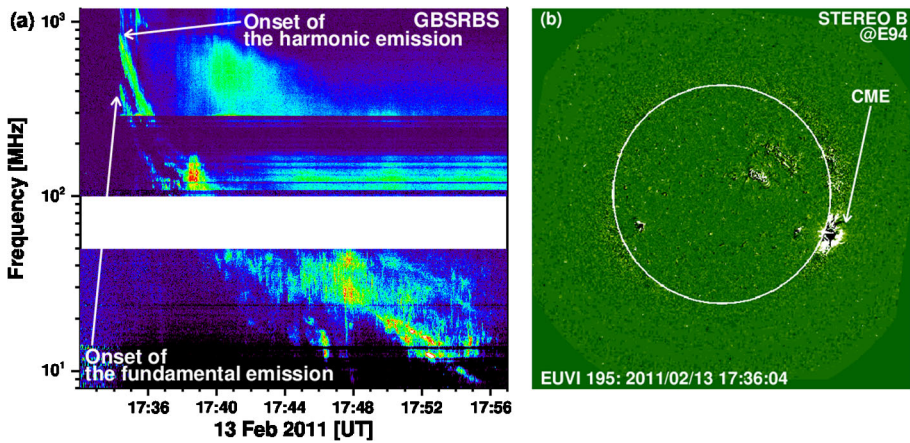
Figure 1 (**a**) A high-starting-frequency type II burst. The dynamic spectrum was obtained by the Green Bank Solar Radio Burst Spectrometer (GBSRBS). The fundamental starting frequency was 420 MHz at 17:35:00 UT. The high starting frequency implies the radio source closer to the solar surface, hence the associated CME originating in the lower corona. (**b**) STEREO-B/EUVI 195 Å difference image shown by white arrow. The time of the image in (**b**) is close to the starting time of the type II burst. STEREO-B was located at E94 at the time of the eruption.

60 MHz (f1) at 17:40:30 UT (t1). According to Equation 1, the corresponding drift rate is −1.09 MHz/sec. The event was associated with a flare, which occurred at N20E04 on the solar disk (see Cho et al., 2013, for details). The associated CME was at N20W90 in the STEREO-B EUVI field of view (FOV). The CME-driven shock was observed in EUV 64 seconds after the appearance of type II burst corresponding to a height of 1.22 Rs.

The relationship between the starting frequency of type II bursts in Solar Cycle 24 with the corresponding CME shock height can be obtained using the procedure in Gopalswamy et al. (2013).

2.1. Multispacecraft measurements of the CME speed and height

The spatial and temporal characteristics of the CMEs associated with type II bursts have been analyzed previously using STEREO data (Gopalswamy et al., 2009a). The events having a clear CME images available in the coronagraph or EUV near the type II onset are considered for shock analysis. When the eruption is near the limb, the CME leading edge was measured in coronagraph/EUV images nearest to the type II burst onset and the height obtained was considered as the shock height as described in Gopalswamy et al. (2013). The wave diameter method was used for CMEs that erupted on the solar disk. By fitting a circle to the outer edge of the disturbance near the time of the type II onset, the shock height was considered as the radius of the circle (Gopalswamy et al., 2013). The CME speeds were obtained by a linear fitting of STEREO/COR1 or SOHO/LASCO height–time data.

3. Results and discussion

3.1. Statistical results

Type II, CME, and flare properties of each event in this study are compiled in Table 1. The second column lists the date (yy:mm:dd format) and universal time (hh:mm:ss for-

Table 1 Type II SRB parameters with the associated solar transients.

SN	Type II (UT)	fs (MHz)	$\frac{\Delta f}{\Delta t}$ (MHz/s)	CME (UT)	v1 (km/s)	v2 (km/s)	v_{DS} (km/s)	v_{II} (km/s)	Width (deg)	r (Rs)	Flare (UT)	Flare Loc	Flare Class
1	20100318 23:11:58	75	−0.20	23:11:00	488	1005	1216	820	79	2.50	22:56	N19W57	B7.0
2	20100612 00:56:29	106	−0.47	00:58:08	486	864	979	673	119	1.21	00:30	N23W43	M2.0
3	20100807 16:59:10	86	−0.083	18:08:00	871	559	275	708	360	1.56	17:55	N11E34	M1.0
4	20100814 09:52:35	58	−0.23	09:55:30	1205	1137	1432	1230	360	1.98	09:36	N17W54	C7.0
5	20101016 19:14:43	86	−0.32	19:15:30	374	772	1100	810	17	1.62	19:09	S20W26	M2.9
6	20110127 12:08:36	43	−0.068	12:08:00	349	461	430	603	47	1.49	12:00	S14W84	C1.2
7	20110128 01:02:30	76	−0.24	01:02:10	606	637	749	650	119	1.30	00:48	S16W84	M1.3
8	20110228 07:40:11	113	−0.37	07:40:09	–	680	711	385	32	1.19	07:34	N23E45	C2.4
9	20110308 03:44:00	80	−0.35	03:44:10	732	1036	1165	1370	260	1.46	03:36	S21E72	M1.5
10	20110325 23:17:119	125	−0.25	23:15:55	–	526	504	568	54	1.38	23:08	S12E45	M1.0
11	20110511 02:27:51	74	−0.05	02:30:30	745	550	178	893	225	1.44	02:23	N19W51	B8.1
12	20110530 11:07:07	80	−0.09	11:10:00	288	581	285	812	95	1.39	10:48	S18E60	C2.8
13	20110711 10:50:19	61	−0.082	10:51:04	267	515	466	418	35	1.90	10:47	S17E06	C2.6
14	20110828 04:20:00	90	−0.20	04:20:08	433	535	559	847	72	1.38	04:17	N23W73	B5.4
15	20110906 22:19:31	131	−0.40	22:20:09	575	876	774	1032	360	1.39	22:20	N14W18	X2.1
16	20110929 12:55:29	53	−0.030	13:00:00	–	298	230	441	73	2.23	12:47	N10W11	C2.7
17	20110930 19:07:54	32	−0.023	19:10:56	339	532	253	314	14	1.93	18:48	N08E08	M1.0
18	20111001 09:55:15	80	−0.20	09:55:30	448	577.5	643	974	203	1.41	08:48	N16W45	C2.8
19	20111114 09:23:17	84	−0.31	09:25:30	331	941	1010	880	62	1.50	09:18	N20W61	C5.2
20	20111117 07:28:09	92	−0.24	07:27:00	458	751	714	780	97	1.50	07:27	S19E08	C6.0
21	20111119 01:27:15	90	−0.20	01:29:00	507	612	588	560	57	1.45	01:21	N21W69	C1.0
22	20111125 21:54:57	125	−0.20	22:00:00	260	517	385	302	66	1.32	21:49	N17W62	C2.4
23	20120118 23:23:11	45	−0.041	23:28:00	270	494	254	406	119	1.53	22:57	N30E31	C5.1
24	20120119 12:53:15	43	−0.048	13:00:00	498	514	413	1021	65	2.03	12:41	N24W55	C3.2

Table 1 (*Continued.*)

SN	Type II (UT)	fs (MHz)	$\frac{\Delta f}{\Delta t}$ (MHz/s)	CME (UT)	v1 (km/s)	v2 (km/s)	v_{DS} (km/s)	v_{II} (km/s)	Width (deg)	r (Rs)	Flare (UT)	Flare Loc	Flare Class
25	20120424 07:48:11	45	−0.096	07:48:00	443	613	588	800	190	1.51	07:38	N12E83	C3.7
26	20120517 01:33:49	75	−0.26	01:30:31	1582	1503	999	2220	360	1.58	01:25	N11W76	M5.1
27	20120601 22:33:04	34	−0.061	22:30:30	630	613	583	684	175	1.78	22:30	N14W76	C3.3
28	20120608 03:08:04	90	−0.053	03:47:14	353	492	142	673	119	1.32	03:07	S19W21	C7.7
29	20120702 05:10:15	90	−0.23	06:00:04	251	433	634	626	90	1.36	05:01	N17E10	C3.5
30	20120703 20:48:10	41	−0.042	20:48:00	294	553	374	800	72	2.00	20:36	S18W07	C9.3
31	20120706 11:07:17	62	−0.150	11:09:00	218	646	675	312	62	1.53	10:24	S17W42	M1.8
32	20120727 17:30:57	43	−0.053	17:31:00	393	578	418	905	114	1.86	17:17	S18E62	M2.7
33	20120731 00:01:16	46	−0.065	00:05:31	486	547	467	870	198	1.81	–	–	–
34	20120731 17:31:36	71	−0.105	17:35:31	–	540	505	673		1.87	17:10	S25E21	C4.0
35	20120915 22:59:30	98	−0.12	23:00:07	184	380	288	557	79	1.27	22:53	N28W76	B9.6
36	20120925 04:29:31	81	−0.084	–	–	–	–	–	–	–	04:24	N09E20	C3.6
37	20121108 02:21:39	63	−0.109	02:21:29	855	794	552	974	360	1.75	02:08	N18E85	M1.7
38	20121112 23:29:26	87	−0.122	23:35:31	–	645	450	296	39	1.76	23:13	S25E47	M2.0
39	20121116 15:39:58	86	−0.300	15:40:09	325	746.5	795.5	788	51	1.25	15:34	N09E78	C8.4
40	20130330 13:23:06	55	−0.069	13:25:37	106	343	362	465	17	1.58	–	–	–
41	20130411 07:02:43	75	−0.18	07:24:06	861	906	657	1096	360	1.50	06:55	N09E12	M6.5
42	20130423 18:23:47	42	−0.063	18:23:00	403	460	430	568	106	1.57	18:10	S20W73	C3.0
43	20130428 20:20:03	43	−0.080	20:20:30	497	585	583	1102	91	1.72	20:10	S18W37	C4.4
44	20130429 19:35:58	43	−0.088	19:35:00	239	628	646	661	61	1.73	19:26	S18W51	C4.0
45	20130502 05:07:28	77	−0.121	05:05:31	671	654	462	1183	99	1.61	04:58	N10W26	M1.1
46	20130517 08:50:31	88	−0.16	09:12:10	1345	983	484	684	360	1.46	08:43	N12E57	M3.2
47	20130531 19:58:20	77	−0.050	–	172	–	–	–	52	–	19:52	N13E43	M1.0
48	20130602 14:52:24	72	−0.212	14:52:00	311	657	645	719	25	1.20	14:47	N12E20	B3.7

Table 1 (*Continued.*)

SN	Type II (UT)	fs (MHz)	$\frac{\Delta f}{\Delta t}$ (MHz/s)	CME (UT)	v1 (km/s)	v2 (km/s)	v_{DS} (km/s)	v_{II} (km/s)	Width (deg)	r (Rs)	Flare (UT)	Flare Loc	Flare Class
49	20130919 19:47:38	49	−0.045	19:50:39	464	444	293	661	257	1.75	19:48	N10E45	B6.0
50	20131005 07:00:00	110	−0.49	06:52:00	964	1176	1178	1450	360	1.45	06:45	–	–
51	20131011 07:13:01	92	−0.22	07:24:10	1200	797	598	964	360	1.37	07:25	N21E103	M1.5
52	20131016 09:19:20	72	−0.063	–	–	–	–	–	–	–	09:10	S11W41	C1.8
53	20131025 03:00:39	61	−0.053	03:05:51	344	503	301	672	121	1.90	02:48	N07E78	M2.9
54	20131025 08:00:16	120	−0.32	08:12:05	587	671	657	893	360	1.35	07:53	S08E73	X1.7
55	20131025 13:36:23	84	−0.130	–	–	–	378	893	–	1.34	13:30	S6W38	C2.3
56	20131102 04:46:35	135	−0.355	04:45:53	828	784	580	1069	360	1.21	04:40	S23W04	C8.2
57	20131107 14:25:28	135	−0.275	–	411	–	–	–	360	–	14:15	S14E23	M2.4
58	20131119 10:25:03	74	−0.138		740	852	531	1020	360	1.56	10:14	S70W14	X1.0
59	20131207 07:24:28	125	−0.44	07:27:00	1085	1087	1027.5	1276	360	1.60	07:17	S16W49	M1.2
60	20131212 03:19:45	85	−0.33	03:36:05	1002	1089	1147	1100	276	1.62	03:11	S23W46	C4.6
61	20140126 08:35:28	52	−0.27	08:36:05	1088	1993.5	2441	2368	255	2.50	08:26	S17E88	C1.5
62	20140220 03:22:15	66	−0.110	03:25:57	993	976	581	615	360	1.91	03:15	S14E38	C3.3
63	20140224 14:53:06	87	−0.313	14:52:00	266	673	919	793	83	1.40	14:44	S11E63	C5.0
64	20140306 09:26:38	109	−0.17	10:12:05	252	374	395.5	476	61	1.39	09:18	S07E64	–
65	20140320 04:00:52	55	−0.050	03:55:48	740	548	248	590	360	1.50	03:42	S14E35	M1.7
66	20140515 20:30:43	33	−0.076	20:20:00	655	713	912	754	275	2.17	–	–	–
67	20140801 18:18:14	38	−0.063	18:20:18	789	736	644	812	360	2.13	17:55	S10E11	M1.5
68	20140824 12:22:38	40	−0.038	12:15:52	551	701	265	1054	360	1.53	12:00	S07E75	M5.9
69	20140907 02:01:31	94	−0.111	02:05:26	487	509	371	505	104	1.72	01:53	S17E63	C7.5
70	20140923 23:16:03	87	−0.101	23:16:04	331	427	290	520	134	1.37	23:03	S13E33	M2.3
71	20140928 02:45:54	96	−0.09	03:24:05	215	217	231	493	60	1.35	02:39	S13W23	M5.1
72	20141002 18:59:07	91	−0.171	18:58:00	513	620	686	525	159	2.00	18:49	S17W82	M7.3

Table 1 (*Continued.*)

SN	Type II (UT)	fs (MHz)	$\frac{\Delta f}{\Delta t}$ (MHz/s)	CME (UT)	v1 (km/s)	v2 (km/s)	v_{DS} (km/s)	v_{II} (km/s)	Width (deg)	r (Rs)	Flare (UT)	Flare Loc	Flare Class
73	20141024 07:55:29	42	−0.052	07:55:00	677	757	605	1044	96	2.68	07:37	S19W06	M4.0
74	20141105 09:43:38	138	−0.190	09:43:00	386	641	372	609	182	1.48	09:48	N20E68	M7.9
75	20141205 06:09:28	49	−0.068	–	534	–	–	–	172	–	05:57	S21W69	C1.8
76	20141217 04:42:53	38	−0.029	05:00:00	587	613	397	593	360	2.85	04:25	S20E09	M8.7
77	20150309 23:41:59	103	−0.103	23:36:07	–	1007	248	928	160	1.36	23:36	S18E45	M5.8
78	20150311 16:24:13	136	−0.224	16:23:00	240	532	346	638	74	1.15	16:11	S17E22	X2.1
79	20150412 23:37:33	44	−0.090	23:35:00	678	778	840	894	175	2.25	23:24	S14W30	C6.4
80	20150518 14:27:27	46	−0.026	14:36:00	357	426	253	812	58	2.45	13:11	N19W50	B6.7
81	20150601 13:38:02	73	−0.071	–	299	–	–	–	45	–	–	–	–
82	20150828 06:30:10	44	−0.045	06:36:00	370	651	474	723	86	2.54	06:17	S13W64	C4.5
83	20151016 13:25:39	87	−0.19	13:25:00	189	456	765	590	83	1.92	13:20	S21E64	C4.3
84	20151017 04:22:43	92	−0.105	–	218	–	–	–	70	–	04:13	S15E75	C2.8
85	20151223 00:36:30	71	−0.125	00:36:00	520	852	437	730	89	1.36	00:23	S22E63	M4.7
86	20160504 13:53:34	74	−0.081	13:53:00	390	553	365	728	134	1.83	13:41	N08W61	C1.3
87	20160516 00:58:56	103	−0.344	–	–	–	–	–	–	–	00:51	N18W18	C1.0
88	20160710 01:01:05	92	−0.32	01:25:44	368	409	863	534	101	1.36	00:53	N11E69	C8.6
89	20100613 05:37:00	156	−0.34	05:38:08	320	348	481	402	33	1.21	05:30	S25W84	M1.0
90	20101103 12:15:00	280	−0.51	12:16:08	241	522	445	336	66	1.34	12:12	S18E98	C4.9
91	20101231 04:23:00	170	−0.31	04:24:09	363	548	399	597	45	1.20	04:18	N12W57	C1.3
92	20110211 21:46:00	200	−0.36	21:45:42	469	549	414	530	114	1.26	21:36	N00E90	–
93	20110213 17:35:00	420	−1.09	17:35:43	373	537	578	806	276	1.22	17:36	S20E04	M8.0
94	20110215 01:51:48	151	−0.29	01:52:00	669	842	648	1212	360	1.85	01:48	S21W07	X2.2
95	20110216 14:27:25	176	−0.52	14:23:00	–	469.5	625	551	67	1.16	14:18	S20W31	M1.6
96	20110224 07:36:25	235	−1.23	07:36:01	1186	1155	1165	1023	158	1.22	07:23	N14E87	M3.5

Table 1 (*Continued.*)

SN	Type II (UT)	fs (MHz)	$\frac{\Delta f}{\Delta t}$ (MHz/s)	CME (UT)	v1 (km/s)	v2 (km/s)	v_{DS} (km/s)	v_{II} (km/s)	Width (deg)	r (Rs)	Flare (UT)	Flare Loc	Flare Class
97	20110607 06:29:15	151	−0.27	06:25:30	1255	1088	584	824	360	1.79	06:19	S21W54	M2.5
98	20110804 03:52:22	239	−1.39	03:54:0	1315	1134.5	1358	1263	360	1.28	03:41	N19W36	M9.3
99	20110809 08:03:05	158	−0.412	08:05:32	1610	919	871	1340	360	1.83	07:48	N17W69	X6.9
100	20110906 01:45:56	149	−0.38	01:46:02	782	644	596	882	360	1.28	01:35	N14W07	M5.3
101	20120127 18:11:10	186.5	−0.74	18:10:30	2508	1067	898	1100	360	1.24	17:37	N27W71	X1.7
102	20120307 00:20:26	151	−0.45	00:16:13	2684	1043	946	1960	360	1.74	00:02	N17E27	X5.4
103	20120603 18:00:01	155	−0.41	17:53:00	605	720	666	690	180	1.38	17:48	N16E38	M3.3
104	20120606 20:04:30	185	−0.39	20:05:30	494	520	492	812	173	1.28	19:54	S19W05	M2.1
105	20120704 16:43:23	182	−0.32	16:42:00	662	653.5	423	1137	360	1.32	16:33	N14W34	M1.8
106	20120704 22:08:46	179	−0.85	22:10:31	556	1105	1187	848	59	1.37	22:03	S16W29	M4.6
107	20120706 23:09:31	188	−0.29	23:10:30	1828	987	386	1294	360	1.37	23:01	S14W60	X1.1
108	20120708 16:31:05	152	−0.57	16:30:00	1572	1096	1225	835	157	1.79	16:23	S17W74	M6.9
109	20120731 17:27:08	154	−0.37	17:25:00	–	756	815	552	40	1.86	17:24	S25E21	C8.5
110	20120806 04:43:15	148	−0.28	04:43:00	198	514	526	500	46	1.49	04:33	S14E78	M1.6
111	20120813 13:30:13	162	−0.35	12:41:06	435	516	532	522	360	1.35	12:33	N23W03	C2.8
112	20121023 03:17:46	177	−0.32	03:21:00	159	–	416	421	46	1.26	03:13	S15E52	X1.8
113	20130113 08:39:35	155	−0.29	08:40:31	696	646	433	800	46	1.27	08:15	N19W22	M1.7
114	20131106 13:46:35	176	−0.23	13:46:26	347	328	305	415	122	1.28	13:39	S12E37	M3.8
115	20131107 03:40:51	148	−0.29	03:42:09	373	377	654	609	69	1.83	03:34	S14E28	M2.3
116	20140108 03:55:45	240	−0.26	03:48:09	643	672	237	687	108	1.20	03:39	N11W81	M3.6
117	20140211 13:56:55	175	−0.31	13:27:00	330	500	446	426	208	1.38	13:15	S11E11	C8.4
118	20140220 07:47:10	150	−0.25	07:45:31	948	686	526	790	360	1.73	07:24	S15W73	M3.0
119	20140416 19:58:40	181	−0.23	19:58:09	764	678	304	665	61	1.31	19:54	S14E09	M1.0
120	20140418 12:53:55	152	−0.24	12:55:30	1203	920	449	946	360	1.56	12:31	S20W34	M7.3

Table 1 (*Continued.*)

SN	Type II (UT)	fs (MHz)	$\frac{\Delta f}{\Delta t}$ (MHz/s)	CME (UT)	v1 (km/s)	v2 (km/s)	v_{DS} (km/s)	v_{II} (km/s)	Width (deg)	r (Rs)	Flare (UT)	Flare Loc	Flare Class
121	20140425 00:23:51	180	−0.15	00:25:31	456	549	198	893	296	1.30	00:17	S15W90	X1.3
122	20140509 02:21:12	175	−0.25	02:21:01	1099	883	360	1322	360	1.38	–	–	–
123	20140610 11:43:24	162.5	−0.29	11:40:50	925	704	439	1323	111	1.35	11:36	S15E80	X2.2
124	20140822 00:07:36	155	−0.44	23:55:56	–	724	922	605	–	1.78	–	N07E32	C8.5
125	20141030 22:59:54	183	−0.25	–	327	411	–	–	132	–	22:54	S06E66	C4.8
126	20150317 23:32:34	145	−0.34	–	510	–	–	–	110	–	22:49	S21W56	M1.0
127	20150822 06:50:49	144	−0.29	06:50:08	547	831	698	752	360	1.90	06:39	S15E20	M1.2
128	20151104 12:04:15	179	−0.45	–	283	337	–	–	64	–	11:55	N12W73	M2.5

$\frac{\Delta f}{\Delta t}$ = Drift rate.

f_s = Starting frequency of type II bursts.

v1 = Average CME speed within LASCO FOV.

v2 = Average CME speed within STEREO/COR1 and EUVI.

v_{DS} = Average CME speed derived using parameters from dynamic spectra.

v_{II} = Average CME speed at type II onset.

r = CME shock heights at type II onset.

Loc = Solar flare heliographic coordinates.

UT = Universal time.

Rs = Solar radii.

mat). The starting frequencies (fs) of the type II bursts are given in column 3. The type II bursts drift rate ($\frac{\Delta f}{\Delta t}$) in the metric range obtained from the dynamic spectra available at https://cdaw.gsfc.nasa.gov/meetings/2017_mekelle/00_all_type2.html are given in column 4. The CME time (hh:mm:ss format) is given in column 5. Columns 6 and 7 list the CME average speed within the LASCO (v1) and the STEREO/COR1 and EUVI (v2) FOVs, respectively. They are obtained based on a linear fit to the height–time measurements in the respective FOVs. SDO/AIA measurements were checked for confirmation. The average speeds of LASCO CMEs are listed in https://cdaw.gsfc.nasa.gov/CME_list/. Column 8 shows the shock speed (v_{DS}) derived from the dynamic spectra. We used Equation 1 to estimate the shock speeds, using $\alpha = 7.63$ derived in this study. Column 9 lists the CME speeds (v_{II}) at the first appearance of type II. One can get information regarding CME acceleration or deceleration after the shock by comparing the CME average speeds (v2) and CME shock speeds (v_{II}) at type II onset. The CME widths are listed in column 10 and their shock heights (r) at type II onset are given in column 11. Columns 12, 13 and 14 show the flare occurrence time, heliographic coordinates and the GOES soft X-ray flare classes, respectively.

3.2. Type II burst properties and CME characteristics

Figure 2(a) shows the distribution of the starting frequencies of type II bursts with mean and median values 110 and 94 MHz, respectively. Our results are similar to previous results obtained in Gopalswamy et al. (2013) for a smaller sample. Figure 2(b) shows the distribution of the drift rate, which has a mean of 0.24 MHz/s and a median of 0.22 MHz/s. The CME heights range from 1.15 to 2.85 Rs (see column 11 of Table 1). Figure 2(c) shows the distribution of CME heights for the 117 type IIs in which the shock could be observed. The obtained mean and median values are 1.59 and 1.49 Rs, respectively. For the 37 events with high starting frequencies, the CME heights range from 1.16 to 1.90 Rs (the shock was observed for 37 bursts out of 40). Their mean and median shock heights are 1.44 and 1.34 Rs, respectively. The mean shock height is reduced to 1.59 Rs by considering all analyzed events, and this is consistent with previous results. Figure 3 shows the scatter plot between the starting frequencies and CME radial distances for different data sets. By considering the higher-starting-frequency bursts presented in Figure 3(a), the relationship between the starting frequency with the CME radial distances can be fit with a power law of the form $f(r) = 175.028r^{-4.501} + 137.297$, this implies that the plasma density varies as $r^{-9.002}$, which is consistent with previous studies (Newkirk, 1967; Saito, 1970; Leblanc, Dulk, and Bougeret, 1998). For lower-starting-frequency bursts, the data could be fit with $f(r) = 127.047r^{-2.510} + 33.031$ (Figure 3(b)). By comparing the two equations, we found that the power-law index increases from higher to lower frequencies. By combining the two data sets in Figure 3(c), the coronal density drops off steeply with the distance. Our result is similar to the results obtained in Gopalswamy et al. (2013) and consistent with the power-law index of ~ 6 derived from eclipse observations (Allen, 1947; Newkirk, 1967). Excluding the highest starting frequency burst in Figure 3(d), the correlation coefficient increases to 0.53 and the coronal-density power-law exponent increases also. The obtained correlation coefficients are significant, but not good because the data considered corresponds to different days over 6 years period, hence the coronal densities are expected to be different. In this study, the high-starting-frequency events are associated with shocks closer to the surface. This may indicate propagation of the shock through a high-density magnetic structure (Pohjolainen, Pomoell, and Vainio, 2008; Cho et al., 2013). The shock heights of CMEs associated with low-frequency events are generally large, which confirms the results of the previous study by Gopalswamy et al. (2013).
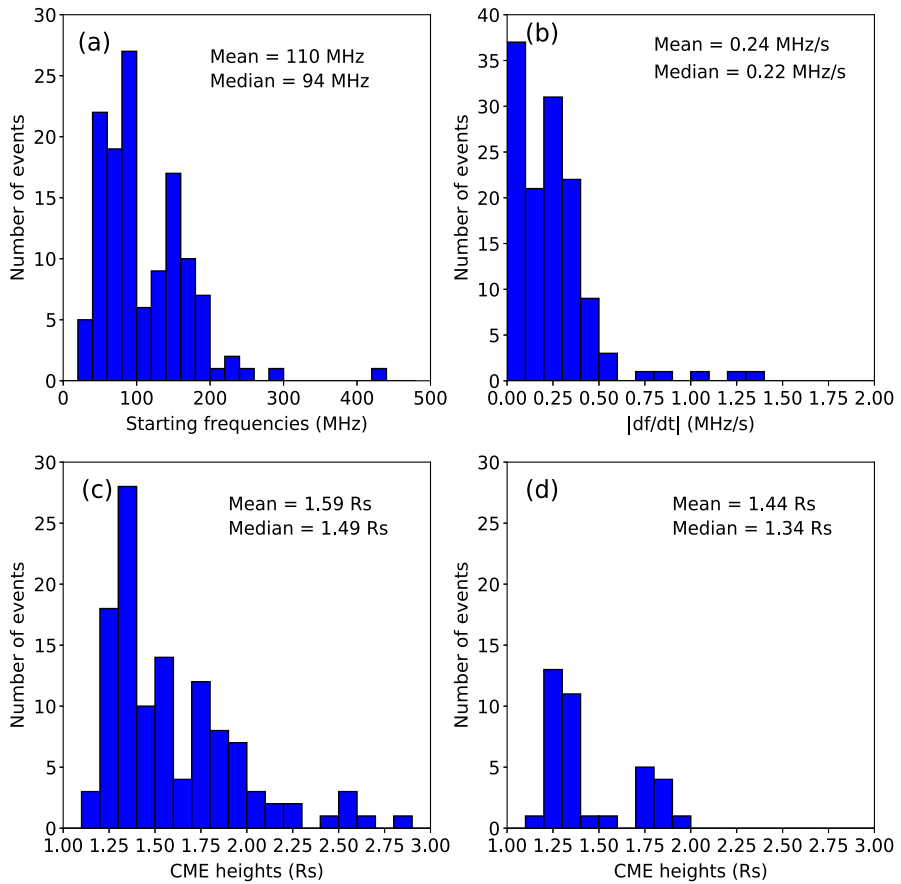
Figure 2 (**a**) Starting frequencies of type II bursts. Here the starting frequencies of the fundamental mode were considered for all analyzed events. The mean and median values are shown on the plot. (**b**) Type II bursts drift rate. More events have low drift rate (≥ 0.2). The mean of the drift rate is 0.24 MHz/s. (**c**) CME heights at the first appearance of type II bursts for all analyzed events. (**d**) Distribution of CME heights at the time of type II burst for events having the starting frequency of the fundamental mode greater than or equal to 150 MHz. The shock heights for high starting events are smaller and consistent with previous results.

Figure 4(a) shows a scatter plot between the drift rate ($\frac{\Delta f}{\Delta t}$) and starting frequency (fs) for the high-frequency type II bursts with an observed fundamental–harmonic (F–H) structure. The line in the scatter plot represents a power law of the form $\mid \frac{\Delta f}{\Delta t} \mid \sim f^{1.19}$. The exponent $\epsilon = 1.19$ is smaller than 1.89, as obtained by considering starting frequencies down to 18 MHz (Vršnak et al., 2001). A similar analysis made by Aguilar-Rodriguez et al. (2005) found ϵ of 1.44. Gopalswamy et al. (2009a) combined 10 bursts with the 58 reported by Mann et al. (1996) and found ϵ of 1.27 with the starting frequencies ranging between $\sim$ 220 and 40 MHz. Figure 4(b) presents the frequency–drift rate relationship for the 88 low-starting frequency bursts, for which the value of ϵ increases to 1.49. For this case, the frequencies range between 138 and 32 MHz. From the observations, the power-law index increases from m to km frequency domains, which implies the decrease of plasma density and speed. Combining the high- and low-starting-frequency type II bursts, we see that the power-law index is higher than for high-starting-frequency events and ones lower than the
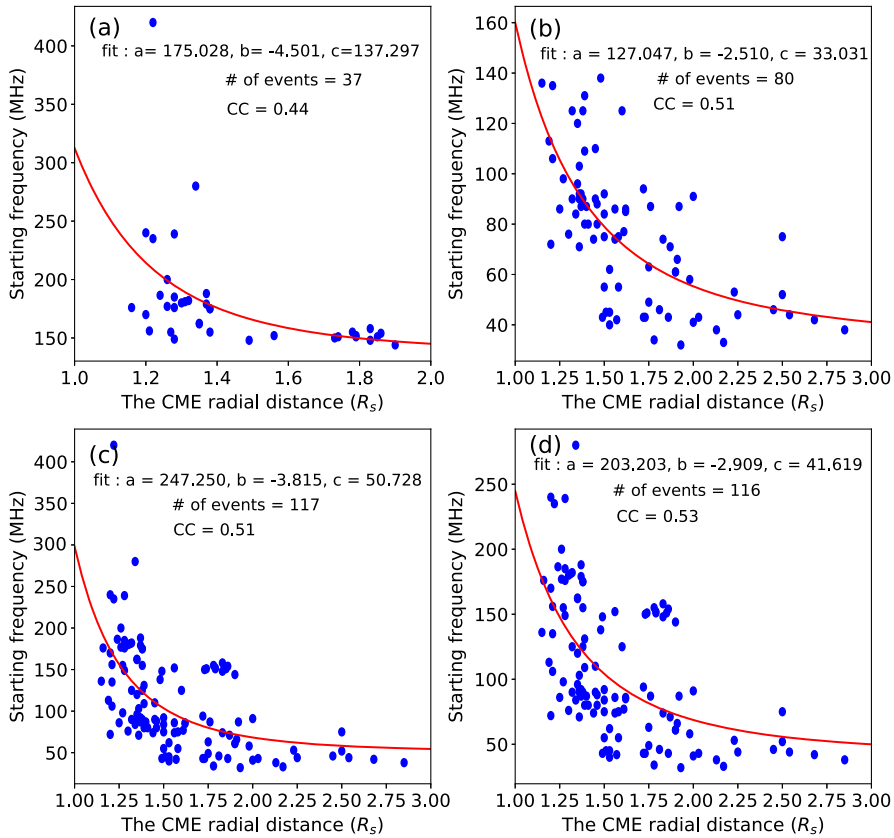
Figure 3 (**a**) Scatter plot between CME heights and the high-starting-frequency type II burst with a power-law fit to the data. (**b**) Scatter plot between CME heights and type II starting frequency for low-starting-frequency events. (**c**) Scatter plot between CME heights and the starting frequency of type II for all events (i.e., combined data of low- and high-starting-frequency type II bursts). The correlation coefficient (CC) is 0.51. Excluding the highest starting frequency (**d**), the correlation coefficient becomes 0.53.

low-starting-frequency events (see Figure 4(c,d)). Combining the 10 metric type II bursts from Gopalswamy et al. (2009a) with the 128 metric type II analyzed in this study, the power-law index becomes 1.33, which is consistent with the considered frequency range of 420 and 32 MHz. Current analysis thus confirms the existence of some deviations from the universal relationship between starting frequency of type II and drift rate. The deviation happens because the shock speed changes within the corona and in the interplanetary medium following the CME speed evolution.

3.3. Characteristics of CME average and shock speeds

The estimated average and median speeds of the CMEs within the STEREO/COR1 and EUVI FOV for all events are 705 and 645 km/s, respectively. The average and median speeds derived from the dynamic spectra (602 and 525 km/s, respectively) are slightly smaller than the corresponding CME speeds. From calculations, it was found that some type II bursts originating near the solar disk center have low drift rates resulting in smaller speeds compare to their corresponding speeds of the CME. Shock flank propagates with a slower speed
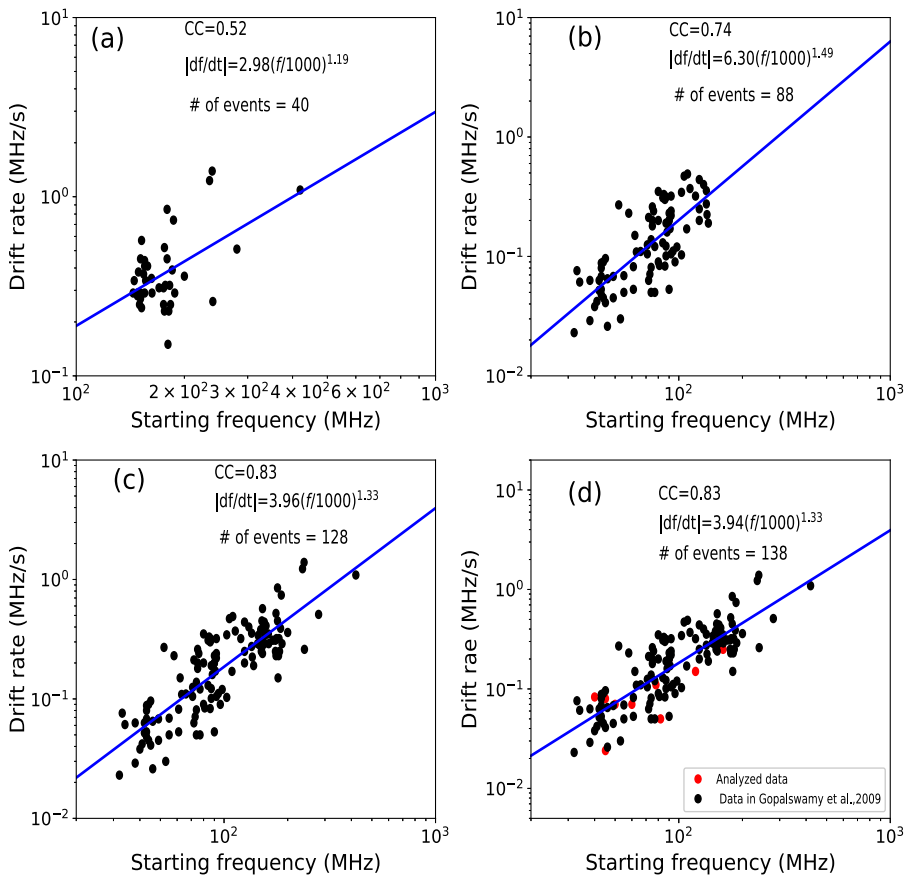
Figure 4   (**a**) Scatter plot between the starting frequency f and the drift rate df/dt (absolute value) for the 40 high starting frequency metric type II burst, the scatter plot represent a power law of the form $|df/dt| \sim f^{\epsilon}$ with $\epsilon = 1.19$. (**b**) A similar plot for the 88 events with lower starting frequency, the power-law index (ϵ) increases to 1.49. The combined set of 128 type II bursts in Figure (**c**) gives $\epsilon = 1.33$. (**d**) The superposition of 10 data points reported in Gopalswamy et al. (2009a) with 128 data points analyzed in this study. ϵ remains 1.33.

than the CME leading edge, but the electron acceleration at the flanks might be more efficient because of the more perpendicular shock angle. For example, for the type II burst that occurred on 2012 May 17, the estimated shock height was 1.58 Rs and its starting frequency was 75 MHz, however, the drift was 0.26 MHz/s, which corresponds with a speed of 999 km/s. Figure 5 depicts distributions of speeds v1, v2, v_{DS} and v_{II}. The average and median CME speeds within the LASCO FOV (640 and 494 km/s, respectively) are close to the average CME speeds found within the STEREO/COR1 and EUVI and average CME speed derived using dynamic spectra. The speeds are larger than the general population of CMEs ($\sim$ 480 km/s in Gopalswamy, 2006b). The average and median shock speeds at type II onset are higher (834 and 791 km/s, respectively) compared to the average speeds obtained by linear fitting the height–time measurements in the STEREO and LASCO FOVs. The high shock speed is consistent with the requirement that shocks are capable of acceler-
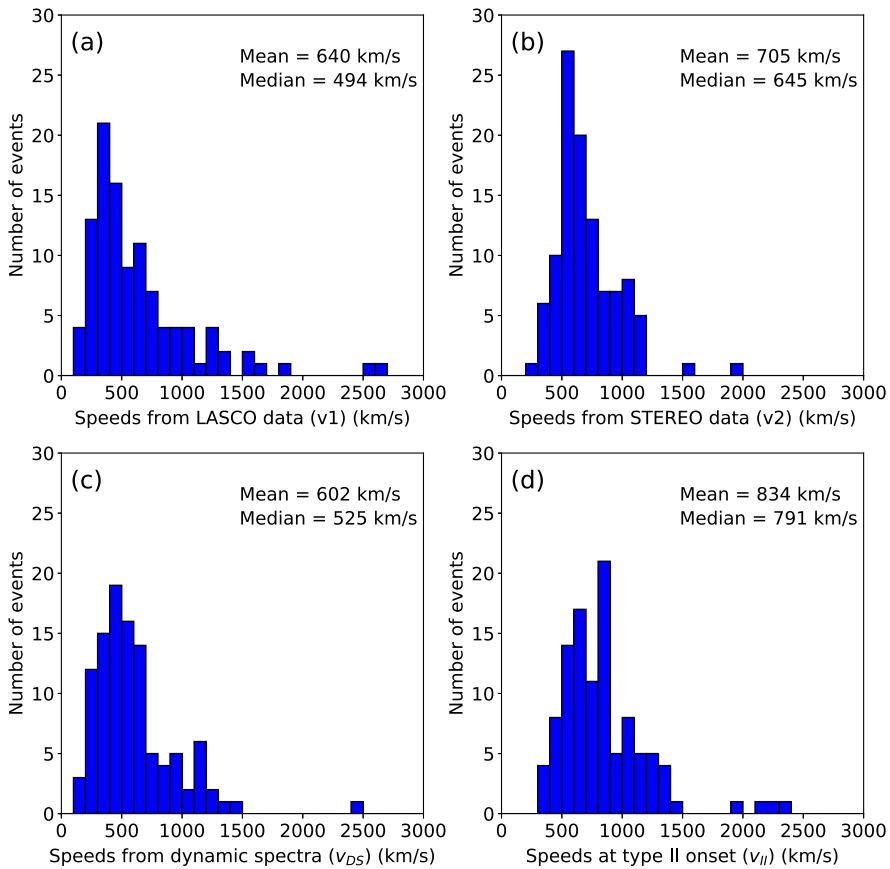
Figure 5 (**a**) Distribution of CME speeds within the LASCO FOV. The average and median CME speeds in the LASCO FOV are 640 and 494 km/s, respectively. (**b**) Distribution of CME speeds within the STEREO FOV, the average and median CME speeds are 705 and 645 km/s, thus higher than the speed in the LASCO FOV and consistent with the shock formation observed in the STEREO FOV. (**c**) Distribution of CMEs speed from the dynamic spectra, the observed average and median are 602 and 525 km/s. The average speed is lower than the speeds in STEREO and LASCO and this may be due to a radio source towards the shock flank, which propagates with a slower speed than the CME leading edge. (**d**) Distribution of CME speeds at type II onset, the obtained shock speed is higher than the average speed within STEREO FOV, which confirms CME acceleration after the appearance of shock.

ating particles. As shown in Figure 5, all the average speeds are greater than their median speeds which implies that the major outliers are located in high end of the distribution.

Figure 6 is the scatter plot between the average CME speeds from STEREO data and the speeds estimated from the dynamic spectra. The correlation coefficient is 0.76 for all events and 0.77 by excluding the two outliers near v2 ∼ 1500 km/s. The obtained correlation is significant. The average width of CMEs in the LASCO FOV is 172°, which is greater than 46° obtained in Gopalswamy (2006b). Since the width is proportional to the mass, this shows that analyzed CMEs associated with type IIs are wide and more energetic. The obtained hierarchical relationship between CME kinetic energy and the wavelength range over which the type II bursts occur is consistent with previous results in Gopalswamy (2006a), Gopalswamy et al. (2009a). Generally, many events are associated with M and C class flares. For
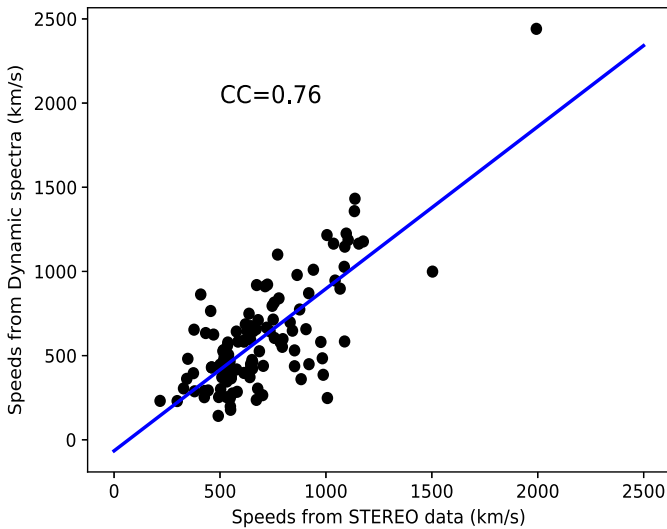
Figure 6 Scatter plot between speeds from STEREO data (v2) and the radio dynamic spectra (v_{DS}). The correlation coefficient (cc) is 0.76. When we exclude the two outliers near v2 $\sim$ 1500 km/s, cc = 0.77.

CMEs associated with high-frequency type II bursts, 33 out of 40 are associated with highly energetic flares (M and X class flares), which is consistent with their speeds. Moreover, there is a clear increase in speed between the inner and outer corona as measured in the STEREO and LASCO FOVs, which shows that the CMEs accelerate at the appearance of the metric type II burst. This has implications for the behavior of drift rate spectrum of type II bursts (Gopalswamy et al., 2009a). For a few events, the shock speeds at the time of metric type II bursts are smaller than the calculated average speeds within the STEREO/COR1 and EUVI FOV, which shows that the CME reached the peak speed before the appearance of type II bursts.

4. Summary

In this study, we used STEREO/COR1, EUVI and SDO/AIA images to identify CME shocks close to the first appearance time of type II bursts and to minimize projection effects. We determined CME heights using both the wave diameter and leading edge methods for 117 of the 128 events for which the shock could be observed. The data period extends from 2010 until 2016, covering the period of SDO operation. Extrapolation was used for a few events where the coronal images close to the onset time of the type II were not available.

We found the CME shock nose to be in the heliocentric distance range from 1.15 to 2.85 Rs, with mean and median values of 1.59 and 1.49 Rs, respectively. The obtained results are consistent with recent findings by Gopalswamy et al. (2013), who analyzed 32 metric type II bursts and found the shock heights in the range 1.20 to 1.93 Rs. In the case of the high-starting-frequency bursts, the shock was formed very near the solar surface between 1.16 to 1.90 Rs, with the mean and median values of 1.44 and 1.34 Rs, respectively. This implies that solar energetic particles are accelerated very close to the coronal base. Making use of type II bursts at different wavelengths, it was found that the power law between the starting frequency and CME heights are consistent with the rapid decline of density in the

inner corona. The density drops from lower corona to the interplanetary medium, in other words the density increases with the increase of the type II emission frequency as it was reported in Gopalswamy et al. (2009a).

We investigated how the high-frequency type II bursts behave with respect to the power-law nature of the drift rate spectrum of type II radio bursts. The power-law exponent is the smallest at the highest frequencies, consistent with the trend in the deviation from the universal drift rate spectrum. Closer to the solar surface, where type II emission frequency is high, the CME speed increases due to fast acceleration and starts to decrease in the IP medium, which shows the relationship between these deviations from the universal drift rate spectrum of type II bursts and CME speeds. The high-starting-frequency type II bursts have high drift rates and are associated with fast CMEs, which is consistent with the CME driving shock regardless of the spectral domain of type II bursts.

Disclosure of Potential Conflicts of Interest   The authors declare that they have no conflicts of interest.

Publisher's Note   Springer Nature remains neutral with regard to jurisdictional claims in published maps and institutional affiliations.

References

Aguilar-Rodriguez, E., Gopalswamy, N., MacDowall, R., Yashiro, S., Kaiser, M.I.: 2005, A study of the drift rate of type II radio bursts at different wavelengths. In: *Solar Wind 11/SOHO 16. Connecting Sun and Heliosphere* **592**, 393. ADS.

Allen, C.W.: 1947, Interpretation of electron densities from corona brightness. *Mon. Not. Roy. Astron. Soc.* **107**, 426. DOI. ADS.

Bougeret, J.-L., Kaiser, M.L., Kellogg, P.J., Manning, R., Goetz, K., Monson, S.J., Monge, N., Friel, L., Meetre, C.A., Perche, C., Sitruk, L., Hoang, S.: 1995, WAVES: the radio and plasma wave investigation on the wind spacecraft. *Space Sci. Rev.* **71**, 231. DOI. ADS.

Cho, K.-S., Gopalswamy, N., Kwon, R.-Y., Kim, R.-S., Yashiro, S.: 2013, A high-frequency type II solar radio burst associated with the 2011 February 13 Coronal Mass Ejection. *Astrophys. J.* **765**, 148. DOI. ADS.

Cliver, E.W., Nitta, N.V., Thompson, B.J., Zhang, J.: 2004, Coronal shocks of November 1997 revisited: the CME type II timing problem. *Solar Phys.* **225**, 105. DOI. ADS.

Ginzburg, V.L., Zheleznyakov, V.V.: 1958, On the possible mechanisms of sporadic solar radio emission (radiation in an isotropic plasma). *Soviet Astron.* **2**, 653. ADS.

Gopalswamy, N.: 2000, Type II solar radio bursts. Radio astronomy at long wavelengths. In: *Geophysical Monograph* **119**, AGU, Washington DC, 123.

Gopalswamy, N.: 2006a, Coronal mass ejections and type II radio bursts. In: Gopalswamy, N., Mewaldt, R., Torsti, J. (eds.) *Solar Eruptions and Energetic Particles*, *American Geophysical Union (Geophysical Monograph Series)* **165**, 207. DOI. ADS.

Gopalswamy, N.: 2006b, Coronal mass ejections of Solar Cycle 23. *J. Astrophys. Astron.* **27**, 243. DOI. ADS.

Gopalswamy, N.: 2011, Coronal mass ejections and solar radio emissions. In: *Planetary, Solar and Heliospheric Radio Emissions (PRE VII)*, 325.

Gopalswamy, N., Lara, A., Kaiser, M.L., Bougeret, J.-L.: 2001a, Near-Sun and near-Earth manifestations of solar eruptions. *J. Geophys. Res.* **106**, 25261. DOI. ADS.

Gopalswamy, N., Yashiro, S., Kaiser, M.L., Howard, R.A., Bougeret, J.-L.: 2001b, Characteristics of coronal mass ejections associated with long-wavelength type II radio bursts. *J. Geophys. Res.* **106**, 29219. DOI. ADS.

Gopalswamy, N., Yashiro, S., Krucker, S., Stenborg, G., Howard, R.A., Bougeret, J.-L.: 2004, Intensity variation of large solar energetic particle events associated with coronal mass ejections. *J. Geophys. Res.* **109**, 12105. DOI. ADS.

Gopalswamy, N., Aguilar-Rodriguez, E., Yashiro, S., Nunes, S., Kaiser, M.L., Howard, R.A.: 2005, Type II radio bursts and energetic solar eruptions. *J. Geophys. Res.* **110**, A12S07. DOI. ADS.

Gopalswamy, N., Thompson, W.T., Davila, J.M., Kaiser, M.L., Yashiro, S., Mäkelä, P., Michalek, G., Bougeret, J.-L., Howard, R.A.: 2009a, Relation between type II bursts and CMEs inferred from STEREO observations. *Solar Phys.* **259**, 227. DOI. ADS

Gopalswamy, N., Yashiro, S., Michalek, G., Stenborg, G., Vourlidas, A., Freeland, S., Howard, R.: 2009b, The SOHO/LASCO CME catalog. *Earth Moon Planets* **104**, 295. DOI. ADS.

Gopalswamy, N., Nariaki, N., Akiyama, S., Mäkelä, P., Yashiro, S.: 2012, Coronal magnetic field measurement from EUV images made by the Solar Dynamics Observatory. *Astrophys. J.* **744**, 72. DOI. ADS.

Gopalswamy, N., Xie, H., Mäkelä, P., Yashiro, S., Akiyama, S., Uddin, W., Srivastava, A.K., Joshi, N.C., Chandra, R., Manoharan, P.K., Mahalakshmi, K., Dwivedi, V.C., Jain, R., Awasthi, A.K., Nitta, N.V., Aschwanden, M.J., Choudhary, D.P.: 2013, Height of shock formation in the solar corona inferred from observations of type II radio bursts and coronal mass ejections. *Adv. Space Res.* **51**, 1981. DOI. ADS.

Leblanc, Y., Dulk, G.A., Bougeret, J.-L.: 1998, Tracing the electron density from the corona to 1 au. *Solar Phys.* **183**(165), 180. DOI. ADS.

Lemen, R.J., Title, A.M., Akin, D.J., Boerner, P.F., Chou, C., Drake, J.F., Duncan, D.W., Edwards, C.G., Friedlaender, F.M., Heyman, G.F., Hurlburt, N.E., Katz, N.L., Kushner, G.D., Levay, M., Lindgren, R.W., Mathur, D.P., McFeaters, E.L., Mitchell, S., Rehse, R.A., Schrijver, C.J., Springer, L.A., Stern, R.A., Tarbell, T.D., Wuelser, J.-P., Jacob Wolfson, C., Yanari, C., Bookbinder, J.A., Cheimets, P.N., Caldwell, D., Deluca, E.E., Gates, R., Golub, L., Park, S., Podgorski, W.A., Bush, R.I., Scherrer, P.H., Gummin, M.A., Smith, P., Auker, G., Jerram, P., Pool, P., Soufli, R., Windt, D.L., Beardsley, S., Clapp, M., Lang, J., Waltham, N.: 2012, The Atmospheric Imaging Assembly (AIA) on the Solar Dynamic Observatory (SDO). *Solar Phys.* **275**, 17. DOI. ADS.

Lengyel-Frey, D., Stone, R.G.: 1989, Characteristics of interplanetary type II radio emission and the relationship to shock and plasma properties. *J. Geophys. Res.* **94**(159), 167. DOI. ADS.

Mann, G., Classen, T., Aurass, H.: 1995, Characteristics of coronal shock waves and solar type II radio bursts. *Astron. Astrophys.* **295**, 775. ADS.

Mann, G., Klassen, A.: 2005, Electron beams generated by shock waves in the solar corona. *Astron. Astrophys.* **441**, 319. DOI. ADS.

Mann, G., Klassen, A., Classen, H.F.T., Aurass, H., Scholz, D., MacDowall, R.J., Stone, R.G.: 1996, Catalogue of solar type II radio bursts observed from September 1990 to December 1993 and their statistical analysis. *Astron. Astrophys.* **119**, 489. ADS.

Nelson, G.J., Melrose, D.B.: 1985, Coronal Loops, Magnetohydrodynamic Waves, Shock Wave Propagation, Type 2 Bursts, Electron Acceleration, H Alpha Line, Interplanetary Medium, Plasma Radiation, Solar Flares. Solar Radiophysics: Studies of Emission from the Sun at Metre Wavelengths, 333–359. ADS.

Newkirk, G. Jr.: 1967, Structure of the solar corona. *Annu. Rev. Astron. Astrophys.* **5**, 213. DOI. ADS.

Pohjolainen, S., Pomoell, J., Vainio, R.: 2008, CME liftoff with high-frequency fragmented type II burst emission. *Astron. Astrophys.* **490**(357), 363. DOI. ADS.

Saito, K.: 1970, *Ann. Tokyo Astron. Obs. Ser. 2* **12**, 53.

Schmidt, J.M., Cairns, I.H., Lobzin, V.V.: 2014, The solar type II radio bursts of 7 March 2012: detailed simulation analyses. *J. Geophys. Res.* **119**, 6042. DOI. ADS.

Vršnak, B., Aurass, J., Magdalenic, J., Gopalswamy, N.: 2001, Band-splitting of coronal and interplanetary type II bursts. I. Basic properties. *Astron. Astrophys.* **377**, 321. DOI. ADS.

Yashiro, S., Gopalswamy, N., Michalek, G., St. Cyr, O.C., Plunkett, S.P., Rich, N.B., Howard, R.A.: 2004, A catalog of white light coronal mass ejections observed by the SOHO spacecraft. *J. Geophys. Res.* **109**, A07105. DOI. ADS.

Zlotnik, E.Y., Klassen, A., Aurass, H., Klein, K.-L., Mann, G.: 1998, Interpretation of harmonic structure in solar type II radio bursts. *Radiophys. Quantum Electron.* **41**, 39. DOI. ADS.